NANO LETTERS
Letter
Cite This: Nano Lett. 2018, 18, 7060−7065
pubs.acs.org/NanoLett

Shell-Protective Secondary Silicon Nanostructures as Pressure-Resistant High-Volumetric-Capacity Anodes for Lithium-Ion Batteries

Jiangyan Wang,[†] Lei Liao,[†] Yuzhang Li,[†] Jie Zhao,[†] Feifei Shi,[†] Kai Yan,[†] Allen Pei,[†] Guangxu Chen,[†] Guodong Li,[†] Zhiyi Lu,[†] and Yi Cui*[,†,‡]

[†]Department of Materials Science and Engineering, Stanford University, Stanford, California 94305, United States
[‡]Stanford Institute for Materials and Energy Sciences, SLAC National Accelerator Laboratory, 2575 Sand Hill Road, Menlo Park, California 94025, United States

Supporting Information

ABSTRACT: The nanostructure design of a prereserved hollow space to accommodate 300% volume change of silicon anodes has created exciting promises for high-energy batteries. However, challenges with weak mechanical stability during the calendering process of electrode fabrication and poor volumetric energy density remain to be solved. Here we fabricated a pressure-resistant silicon structure by designing a dense silicon shell coating on secondary micrometer particles, each consisting of many silicon nanoparticles. The silicon skin layer significantly improves mechanical stability, while the inner porous structure efficiently accommodates the volume expansion. Such a structure can resist a high pressure of over 100 MPa and is well-maintained after the calendering process, demonstrating a high volumetric capacity of 2041 mAh cm^{-3}. In addition, the dense silicon shell decreases the surface area and thus increases the initial Coulombic efficiency. With further encapsulation with a graphene cage, which allows the silicon core to expand within the cage while retaining electrical contact, the silicon hollow structure exhibits a high initial Coulombic efficiency and fast rise of later Coulombic efficiencies to >99.5% and superior stability in a full-cell battery.

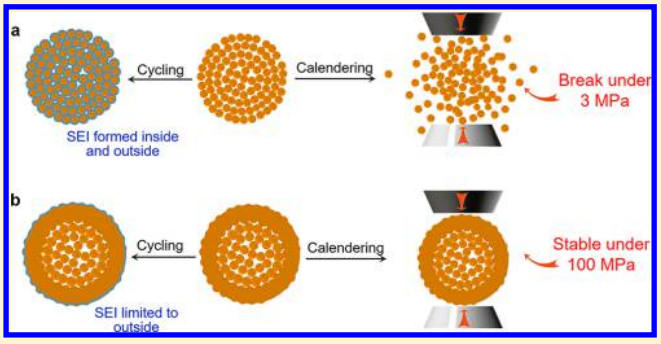

KEYWORDS: *Silicon, shell-protective, calendering, pressure-resistant, high-volumetric capacity, lithium-ion batteries*

Over the past decade, studies on high-capacity silicon anodes through nanostructure design have created exciting promises for high-energy batteries.[1−5] Many challenging issues associated with 300% volume change of silicon anodes have been addressed by structures including nanowires, core−shell, yolk−shell tubes, hollow and porous spheres, pomegranate particles, and new binders.[6−19] An essential concept of these most promising nanostructured silicon anodes is the prereserved hollow space to accommodate a large volume change for reducing the damage to the electrode. However, it remains as a challenge that the void space such as the gap between carbon shell and silicon microparticles and/or the whole nanostructured structure can not survive large mechanical pressure during the calendering process of battery electrode fabrication.[12,14]

The calendering process is an extremely important step of battery electrode fabrication; it packs the electrode materials densely to increase the energy density per volume, improve electrical contact between particles, and increase adhesion between particles and current collector.[20,21] The mechanical pressure during calendering could go up to 80 MPa,[22,23] under which most of hollow nanostructures would break. Thus far, electrode processing of many nanostructures can only utilize no or gentle calendering process, resulting in a low volumetric energy density, poor electric contact, and low areal capacity loading.

Here a pressure-resistant silicon structure was developed through coating a silicon cluster, which is composed of silicon nanoparticles, with a dense layer of silicon shell. The silicon coating layer functions as a strong shell enabling such a structure to resist a high pressure of over 100 MPa. As a result, the structure remains barely broken after the calendering process, achieving an impressive volumetric capacity of 2041 mAh cm^{-3}. Besides, the silicon skin only wraps the outside of the silicon cluster, leaving the inner void space to effectively buffer the volume expansion. In addition, the side reactions are reduced, benefitting from the decreased electrode/electrolyte contact area as a result of the silicon shell coating, resulting in an increased initial Coulombic efficiency. Moreover, after additional coating by a graphene cage, which increases the

Received: July 26, 2018
Revised: October 17, 2018
Published: October 19, 2018

DOI: 10.1021/acs.nanolett.8b03065
Nano Lett. 2018, 18, 7060−7065

conductivity and limits the silicon core to expand toward inside and guarantees the integrity of the whole particle during cycling, the silicon hollow structure exhibits a good stability even in a full-cell battery.

Fabrication and Merits of Shell-Protective Secondary Silicon Nanostructures. The process flow on how we synthesize such a structure is shown in Figure 1a. A bottom-up

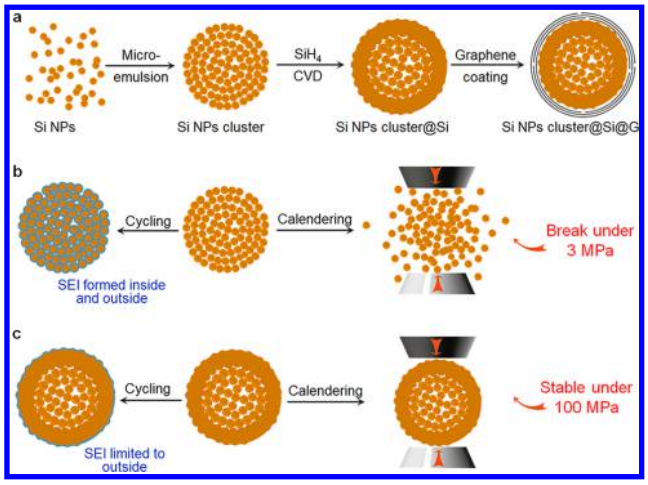

Figure 1. Fabrication and merits of shell-protective secondary silicon nanostructures. (a) Scheme of the fabrication process. (b, c) Comparison of the SEI formation and calendering test between uncoated and Si shell coated Si NPs clusters. (b) Uncoated Si NPs cluster. The electrolyte can diffuse into the inner pores, resulting in excessive SEI formation; the structure collapses easily during the calendering process, resulting in electrical contact loss. (c) After Si shell coating. The electrolyte is prevented from leaking into the interior space, thus restricting SEI formation to the outer surface; more impressively, the structure becomes highly pressure-resistant and maintains intact under 100 MPa.

microemulsion approach[24] was adopted to synthesize micro-sized silicon clusters from silicon nanoparticles. The exterior surface of each silicon cluster was then sealed with a dense silicon shell through a chemical vapor deposition (CVD) method and further encapsulated by a highly conformal graphene cage through the electroless deposition of a Ni template and followed with CVD growth of graphene.[14] After the Ni template was etched away, graphene-encapsulated silicon-shell-protected silicon hollow structures were obtained.

Such a novel design has multiple advantages: (1) the silicon shell significantly improves mechanical stability, rendering the structure able to resist a high pressure of 100 MPa and survive the calendering process (Figure 1b,c). After calendering, both electrical contact and volumetric capacity are improved. (2) The silicon shell also increases the tap density. As demonstrated in Figure S1, the tap density increased from 0.14 g cm^{-3} to 0.47 g cm^{-3} after assembling the nanoparticles into clusters and further increased to 0.79 g cm^{-3} after Si shell coating. (3) The dense silicon shell prevents the electrolyte from diffusing to the interior pores and thus decreases side reactions and SEI formation, improving both the first- and later-cycle Coulombic efficiencies (Figure 1b,c). (4) The inner porous structure provides void space to accommodate the large volume expansion, enabling a good cycling stability. (5) A graphene cage outer coating can improve the conductivity of the whole particle and is mechanically strong and flexible enough to guarantee a stable interfacial layer with an electrolyte and retain structural integrity during cycling.[25]

Morphology and Structure Characterization. The morphology and structure of the products obtained at different steps during the synthesis process are shown in Figure 2. The

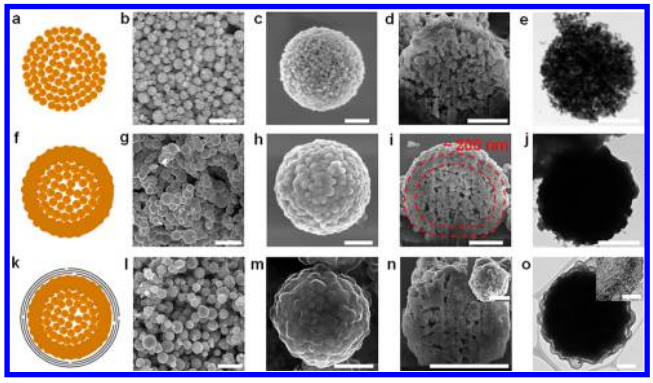

Figure 2. Morphology and structure characterization. Schematic (a, f, k), SEM (b, c, g, h, l, m), FIB-SEM (d, i, n), and TEM (e, j, o) images of Si NPs cluster (a–e), Si NPs cluster@Si microparticles (f–j), and Si NPs cluster@Si@G microparticles. Scale bar for images b, g, and l is 2 μm. Scale bar for other images is 1 μm. Inset in image n is the SEM image of one single Si NPs cluster@Si@G microparticle, showing the surface of the microparticle. Scale bar is 500 nm. Inset in image o is a high-resolution TEM image of the graphene cage's layered structure. Scale bar is 5 nm.

silicon clusters composed of silicon nanoparticles (Si NPs cluster) are highly spherical, ranging from 1 to 5 μm in diameter (Figure 2a–e and Figures S2 and S3) and have many inner pores as clearly demonstrated by the focused ion beam (FIB) scanning electron microscopy (SEM) and transmission electron microscopy (TEM) images. A dense silicon shell is deposited onto each cluster (Si NPs cluster@Si) by CVD treatment. A well-defined silicon shell should be able to sufficiently seal the silicon cluster but still maintain the inner void space. After coating under a low pressure for a short time, both the inside and outside of the cluster are partially coated (Figure S4a,b), allowing the electrolyte to leak into the inside of the cluster from the unsealed pores, thus a low initial Coulombic efficiency (ICE). However, after coating under a low pressure for a long time, both the inside and the outside of the cluster are fully sealed (Figure S4c,d), leaving no void space to buffer the volume expansion, resulting in a poor cycling stability. After coating under a higher pressure for a suitable time, the surface of the cluster is totally covered, while the inner pores are barely sealed (Figure 2i and Figure S4g,h), thus preventing the electrolyte leaking in while still allowing the inside pores to buffer the expansion of the structure during repeated charge/discharge cycles. The thickness of the outside silicon shell is ~200 nm, and it only covers the outer layer of the particles, leaving the highly porous nature of the interior maintained. To better improve the electrochemical performance, the Si NPs cluster@Si microparticles were further encapsulated by a graphene cage. Each Si NPs cluster@Si microparticle was first coated with a layer of Ni (Figure S5), which not only catalyzes the growth of graphene at a low temperature but also serves as the sacrificial layer for providing void space. After Ni was etched away by $FeCl_3$ aqueous solution, graphene-encapsulated Si NPs cluster@Si microparticles were obtained as the final product (Si NPs cluster@

DOI: 10.1021/acs.nanolett.8b03065
Nano Lett. 2018, 18, 7060–7065

Si@G) (Figure 2k–o). To better verify the merits of our Si NPs cluster@Si@G microparticles, Si NPs clusters without silicon shell coating and only encapsulated with graphene cage (Si NPs cluster@G) were also prepared (Figure S6). The multilayered structure of the graphene cage can be clearly observed through the high-resolution TEM (HRTEM) images (Figure S6d and the image inserted in Figure 2o). Raman spectroscopy (Figure S7) also reveals the highly graphitic nature of the carbon shell, wherein the pronounced D band with a narrow bandwidth suggests that sufficient defects are present to facilitate Li-ion transport to silicon.[14] Thermogravimetric analysis (TGA) reveals that the graphene cages make up only ~8% of the total mass of the Si NPs cluster@Si@G composite (~11% for Si NPs cluster@G composite) (Figure S8). Here, the lower carbon content compared with previous works[11−13] is presumed to minimize the irreversible trapping of Li ions by graphene structures and improve Coulombic efficiency without sacrificing the specific capacity.

Pressure-Resistant Property Test. As mentioned above, the calendering process during battery electrode fabrication is highly important, which can increase the volumetric energy density, improve electrical contact, and increase adhesion between particles and current collector. Unfortunately, most previous hollow nanostructures suffer from a poor mechanical stability and collapse easily during the calendering process, resulting in a low volumetric energy density, electrical contact loss, poor cycling stability, and limited practical application. In this work, by depositing a dense silicon shell onto each silicon cluster, the particles' mechanical properties are greatly improved (Figures 3 and Figure S9). The uncoated Si NPs clusters partially break under a quite low pressure of 3 MPa (about 20% of the clusters broke down, Figure 3c) and totally collapse under 15 MPa (Figure 3d). Conversely, after coating with a 100 nm silicon shell (Figure S4e,f), the particles hardly break under 15 MPa (Figure 3g); however, about 45% collapse under 60 MPa (Figure 3h). Impressively, after coating with a 200 nm silicon shell, the structure and shape of the particles still remain barely changed even under a much higher pressure of 100 MPa (Figure 3l). In addition, we found that the results hold for a practical calendering process on Si NPs cluster@G microparticles and Si NPs cluster@Si@G microparticles. As shown in Figure S10, the structure of Si NPs cluster@Si@G microparticles remained intact after the calendering process, while Si NPs cluster@G microspheres totally collapsed; it obviously indicates the pressure-resistant superiority of these shell-protective secondary silicon nanostructures and their suitability for the fabrication of high volumetric capacity electrodes.

Electrochemical Characterization. Our novel design of shell-protective pressure-resistant silicon hollow structure demonstrates a remarkable electrochemical performance both in half-cell and full-cell configurations. Type 2032 coin cells were constructed for cycling tests from 0.01 to 1 V (half cell) and 3.0 to 4.2 V (full cell).

The voltage profiles for the first cycle of different structural silicon microparticles electrodes are compared in Figure 4a and Figure S11. All of them exhibited typical electrochemical features of silicon. Impressively, the initial Coulombic efficiency of 90.4% of the Si NPs cluster@Si@G microparticle electrode is superior to that of the other two electrodes (Table S1, 85.6% and 77.4% for Si NPs cluster@Si and Si NPs cluster@G, respectively). It is worth noting that Coulombic efficiency is one of the most important parameters to evaluate

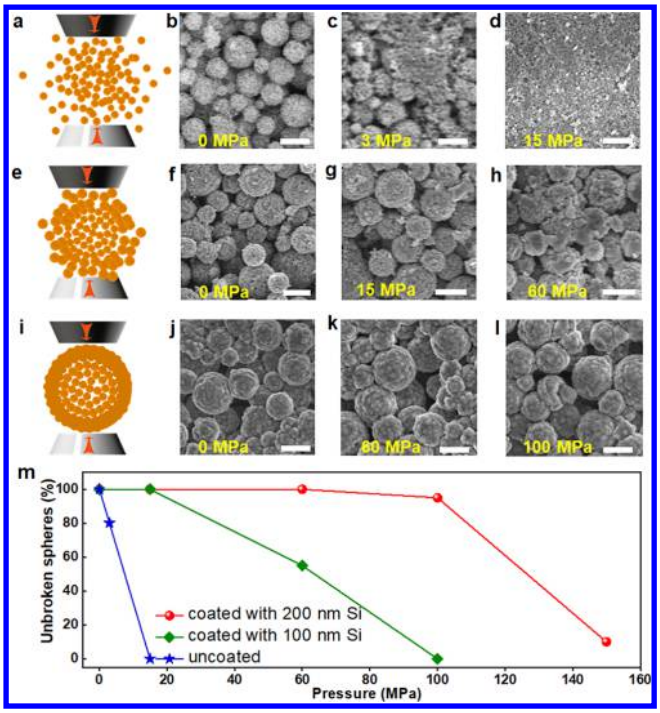

Figure 3. Pressure-resistant property test. (a, e, i) Schematic of (a) uncoated, (e) 100 nm Si skin, and (i) 200 nm Si skin coated Si NPs cluster after calendering. (b–d) SEM images of uncoated Si NP cluster after being pressed under (b) 0 MPa, (c) 3 MPa, and (d) 15 MPa. (f–h) SEM images of 100 nm Si skin coated Si NPs cluster after being pressed under (f) 0 MPa, (g) 15 MPa, and (h) 60 MPa. (j–l) SEM images of 200 nm Si skin coated Si NPs cluster after being pressed under (j) 0 MPa, (k) 60 MPa, and (l) 100 MPa. Scale bar for parts b–d, f–h, and j–l is 2 μm. (m) Diagram of the fraction of unbroken spheres after being pressured as a function of applied pressure.

the performance of a battery, especially those of the early cycles, which account for most of the Li-ion loss and electrolyte consumption. Surprisingly, compared to other high-performing nano-Si anodes that usually need many cycles to reach 99%,[10,12,13,26−30] the Coulombic efficiency of Si NPs cluster@Si@G microparticles is beyond 99% after only 8 cycles (Figure 4c) and is maintained at a high level thereafter (99.5–100%).

There are several characteristics of our pressure-resistant Si hollow structures that contribute to the improvement in early- and later-cycle Coulombic efficiencies: the optimized specific surface area and surface chemistry allows initial SEI formation without consuming too much lithium, and the mechanically stable electrode/electrolyte interface prevents additional SEI formation.[14] First, the silicon shell greatly decreases the surface area accessible by the electrolyte, thus minimizing possible side reactions and irreversible Li consumption. The specific surface area of Si NPs cluster@Si is about five times lower than that of silicon nanoparticles (5.6 vs 29.3 m^2/g) (the actual contact area between uncoated Si NPs cluster electrode and electrolyte is similar to that between Si nanoparticles and electrolyte, given that uncoated Si NPs clusters collapse to nanoparticles after the calendering process), resulting in less SEI formed and higher ICE achieved. Second, different from amorphous carbon coating, which can irreversibly trap lots of Li through the dangling bonds,[12,13] the surface chemistry of graphene cage is similar to that of graphite, making the graphitized carbon

DOI: 10.1021/acs.nanolett.8b03065
Nano Lett. 2018, 18, 7060–7065

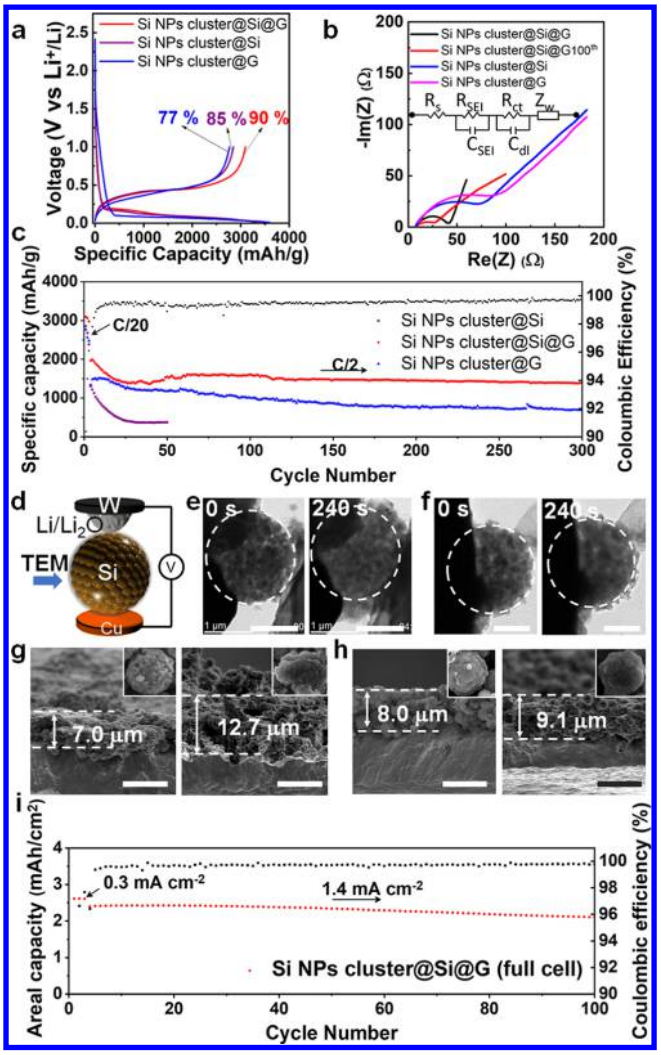

Figure 4. Electrochemical characterization. All of the specific capacities are reported based on the total mass of the active materials (Si and C in the Si NPs cluster@G and Si NPs cluster@Si@G microparticles). (a) First-cycle voltage profiles of individual cells with corresponding Coulombic efficiencies. (b) AC impedance spectra of as-produced Si microparticle film anode for the first cycle. To better evaluate the electrochemical performance of Si NPs cluster@Si@G microparticles, AC impedance spectra for the 100th cycle was also tested. Inserted is the equivalent circuit. R_s reflects a combined resistance of the electrolyte, separator, and electrodes. R_{SEI} and C_{SEI} are the resistance and capacitance of the SEI layer, respectively. R_{ct} and C_{dl} are the charge transfer resistance and double-layer capacitance. Z_w is the Warburg impedance related to a combined effect of Li ions diffusing across the electrode−electrolyte interfaces. (c) Half-cell delithiation capacity of different products. For Si NPs cluster@G and Si NPs cluster@Si@G samples, no conductive additives were added. For bare Si NPs cluster@Si samples, super P was added as a conductive additive. The mass loading of active material was around 0.6 mg cm^{-2}. The rate was C/20 for the initial three cycles and C/2 for later cycles (1C = 4.2 A g^{-1}). The Coulombic efficiency of the Si NPs cluster@Si@G is plotted on the secondary *y*-axis. (d) Schematic of the in situ TEM device. (e, f) Time-lapse images of the lithiation of (e) Si NPs cluster@Si microparticles (also see Movie S1) and (f) Si NPs cluster@Si@G microparticles (also see Movie S2). Scale bar for all of the time-lapse images is 1 μm. (g, h) Cross-sectional SEM images of Si NPs cluster@Si without (g) and with a (h) graphene-encapsulation electrode. Electrodes before (left) and after (right) cycling test, and scale bar is 10 μm. (i) Full-cell delithiation areal capacity of Si NPs cluster@Si@G microparticles (that is the discharge areal capacity of the full cell) paired with a traditional lithium cobalt oxide cathode. The Coulombic efficiency of the Si NPs cluster@Si@G microparticles is plotted on the secondary *y*-axis.

atoms of the cage unlikely to trap Li, thus minimizing irreversible Li consumption. Third, the encapsulation of Si NPs cluster@Si microparticle with mechanically strong graphene cages guarantees a stable electrode/electrolyte interface and prevents additional SEI formation during cycling. Furthermore, electrochemical impedance spectroscopy (EIS) carried out at a voltage of 1.0 V vs Li^+/Li shows that the charge transfer resistance of the Si NPs cluster@Si@G sample is the smallest among the three types of Si-based samples (Figure 4b). It demonstrates that the Si NPs cluster@Si@G microparticle electrode exhibits much faster kinetics than the other electrodes, which may be due to the fact that the optimized specific surface area of Si NPs cluster@Si@G decreases the area accessible by the electrolyte, thus reducing SEI formation and irreversible Li consumption. Besides, it is worth noting that the charge transfer resistance of the Si NPs cluster@Si@G sample only slightly reduces after the 100th cycle, indicating that the SEI layer remains stable during the whole cycling of the Si NPs cluster@Si@G microparticle electrode, enabling high later-cycle Coulombic efficiencies.

The specific capacity and cycling stability are another two very important parameters for the evaluation of a practical battery. As shown in Figure 4c, a reversible capacity of about 3096 mAh g^{-1} at a current density of C/20 (1C = 4.2 A g^{-1}) was achieved by Si NPs cluster@Si@G microparticle electrodes. If not mentioned, all reported capacities are based on the total mass of Si and C in the composite. Considering that silicon is 92% of the mass of the composite, the specific capacity with respect to silicon is as high as 3365 mAh g^{-1}. The volumetric capacity was calculated to be 2041 mAh cm^{-3}, which is about three times the theoretical volumetric capacity of 719 mAh cm^{-3} for graphite anodes[31] and is better than the best results of previously reported silicon-based anodes (Table S2).[9,13,18,32−37] The high capacity indicates that the active materials are electrically well-connected and participate fully in the electrochemical lithiation/delithiation process. Furthermore, a specific capacity of about 1388 mAh g^{-1} was maintained after 300 consecutive cycles at a high rate of C/2, which is still over three times as large as that of commercial graphite anodes' theoretical capacity (372 mAh g^{-1}) and far surpasses that of Si NPs cluster@Si (373 mAh g^{-1} at the 50th cycle) and Si NPs cluster@G (689 mAh g^{-1} at the 300th cycle).

The superior electrochemical stability can be ascribed to two merits of the Si NPs cluster@Si@G composite: (1) the porous inner structure provides void space to accommodate the volume expansion during the cycling; (2) the graphene shell, which acts as a mechanically strong and flexible buffer during deep galvanostatic cycling, limits the microparticles to expand mainly toward the inside and maintains electrical contact, thus improving the cycling stability.

To verify the compatibility of our Si NPs cluster@Si@G structure with the drastic volume expansion of Si lithiation, an in situ TEM study comparing the Si NPs cluster@Si and the Si NPs cluster@Si@G microparticles was performed (Figure 4d−f, Movies S1 and S2). The Si NPs cluster@Si microparticle

DOI: 10.1021/acs.nanolett.8b03065
Nano Lett. 2018, 18, 7060−7065

apparently expands toward both inside and outside during the lithiation process; the random and vigorous expansion finally induces the fracture of the structure. For the Si NPs cluster@Si@G microparticles, the mechanically strong graphene cage limits the inner silicon particle to expand mainly toward the inside and guarantees the integrity of the structure during the whole lithiation process, thus leading to a good cycling stability.

To further investigate the reason for such a good cycling stability, postcycling cross-sectional SEM analyses are carried out to check the morphology change of the silicon electrodes after charge/discharge. As shown by the inserted images in Figure 4g, h, the spherical shape of Si NPs cluster@Si microparticles becomes irregular after cycling, indicating an intensive volume expansion and structural cracking; conversely, Si NPs cluster@Si@G microparticles remain spherical and intact after cycling, indicating a good stability. As verified by dual-beam focused ion beam (FIB) SEM analysis (Figure S13), although the inside pores are reduced after long-term cycling due to the fact that the volume expansion during lithiation cannot be totally released after delithiation, the whole particle maintained a good integrity even after 300 cycles. Moreover, the volume expansion of the Si NPs cluster@Si@G microparticle electrode is calculated to be only 13.7% (~81.4% for Si NPs cluster@Si microparticles), which is superior to that in many reported works,[11,38] indicating a highly successful structure design.

Besides half cells, a full cell with a high mass loading and areal capacity was constructed to better characterize the pressure-resistant property and good cycling stability of the Si NPs cluster@Si@G composite. The areal capacities of the silicon anode and traditional lithium cobalt oxide (LCO) cathode are initially matched (Li-matched). As Figure 4i shows, the Si NPs cluster@Si@G microparticle electrode exhibits stable cycling (2.1 mAh cm^{-2} remained after 100 cycles) and high Coulombic efficiency (99.7% average after the fifth cycle) at a current density of 1.4 mA cm^{-2}. To our knowledge, this areal capacity and Coulombic efficiency are superior to most reported works on silicon-based anode materials.[15]

In summary, we demonstrate a multifunctional silicon shell coating on secondary silicon nanostructures, which not only significantly improves the mechanical stability of silicon structures to be resistant to a high pressure of 100 MPa and achieve a superior volumetric capacity of 2041 mAh cm^{-3} but also decreases the accessible surface area and prevents excessive SEI formation to achieve a highly increased initial Coulombic efficiency. In addition, the silicon shell only wraps the outside surface of the silicon structure, retaining the porous inner structure to provide void space for buffering the volume expansion during the cycling, resulting in an improved cycling stability. After further encapsulation with a graphene cage, which limits the silicon microparticles to expand mainly toward the inside and maintains electrically connected, these shell-protective silicon secondary nanostructures exhibit high Coulombic efficiencies and good stability even in a full-cell battery cycling. This remarkable high volumetric capacity and cycling stability for microsized silicon anode materials demonstrate the promising application of our shell-protective pressure-resistant silicon hollow structures in the lithium battery industry.

■ ASSOCIATED CONTENT

Supporting Information

The Supporting Information is available free of charge on the ACS Publications website at DOI: 10.1021/acs.nanolett.8b03065.

Materials and methods, calculation of the volumetric capacity, calculation of the volumetric energy density, scanning electron microscopy images, Raman spectra, thermogravimetric analysis, voltage profiles, dual-beam focused ion beam (FIB) analysis and cross-sectioned scanning electron microscopy images, galvanostatic half-cell cycling performance, summary of lithium-ion battery performance for different products, and comparison of the volumetric capacity (PDF)

Movie S1 (AVI)

Movie S2 (AVI)

■ AUTHOR INFORMATION

Corresponding Author

*E-mail: yicui@stanford.edu.

ORCID

Jiangyan Wang: 0000-0001-6951-1296

Yuzhang Li: 0000-0002-1502-7869

Jie Zhao: 0000-0001-6446-8313

Allen Pei: 0000-0001-8930-2125

Yi Cui: 0000-0002-6103-6352

Author Contributions

J.W. and L.L. contributed equally. L.L., J.W., and Y.C. conceived and designed the experiments. L.L. and J.W. carried out materials synthesis and electrochemical characterization. J.Z. and F.S. participated in part of the synthesis and materials characterization. Y.L. conducted in situ TEM lithiation and electrical measurements. J.W. wrote the draft of the manuscript. All of the authors discussed the results and commented on the manuscript.

Notes

The authors declare no competing financial interest.

■ ACKNOWLEDGMENTS

Y.C. acknowledges the support from the Assistant Secretary for the Energy Efficiency and Renewable Energy, Office of Vehicle Technologies of the US Department of Energy under the Battery Materials Research (BMR) Program.

■ REFERENCES

(1) Aricò, A. S.; Bruce, P.; Scrosati, B.; Tarascon, J.-M.; van Schalkwijk, W. *Nat. Mater.* **2005**, *4*, 366−377.

(2) Armand, M.; Tarascon, J.-M. *Nature* **2008**, *451*, 652−657.

(3) Dunn, B.; Kamath, H.; Tarascon, J.-M. *Science* **2011**, *334*, 928−935.

(4) Wu, H.; Cui, Y. *Nano Today* **2012**, *7*, 414−429.

(5) Sun, Y.; Liu, N.; Cui, Y. *Nat. Energy* **2016**, *1*, 16071.

(6) Chan, C. K.; Peng, H.; Liu, G.; McIlwrath, K.; Zhang, X. F.; Huggins, R. A.; Cui, Y. *Nat. Nanotechnol.* **2008**, *3*, 31−35.

(7) Cui, L.-F.; Ruffo, R.; Chan, C. K.; Peng, H.; Cui, Y. *Nano Lett.* **2009**, *9*, 491−495.

(8) Zhou, S.; Liu, X.; Wang, D. *Nano Lett.* **2010**, *10*, 860−863.

(9) Yao, Y.; McDowell, M. T.; Ryu, I.; Wu, H.; Liu, N.; Hu, L.; Nix, W. D.; Cui, Y. *Nano Lett.* **2011**, *11*, 2949−2954.

(10) Liu, N.; Wu, H.; McDowell, M. T.; Yao, Y.; Wang, C.; Cui, Y. *Nano Lett.* **2012**, *12*, 3315−332.

DOI: 10.1021/acs.nanolett.8b03065
Nano Lett. 2018, 18, 7060−7065

(11) Yi, R.; Dai, F.; Gordin, M. L.; Chen, S.; Wang, D. *Adv. Energy Mater.* **2013**, *3*, 295−300.
(12) Liu, N.; Lu, Z.; Zhao, J.; McDowell, M. T.; Lee, H.-W.; Zhao, W.; Cui, Y. *Nat. Nanotechnol.* **2014**, *9*, 187−192.
(13) Lu, Z.; Liu, N.; Lee, H.-W.; Zhao, J.; Li, W.; Li, Y.; Cui, Y. *ACS Nano* **2015**, *9*, 2540−2547.
(14) Li, Y.; Yan, K.; Lee, H.-W.; Lu, Z.; Liu, N.; Cui, Y. *Nat. Energy* **2016**, *1*, 15029.
(15) Jin, Y.; Li, S.; Kushima, A.; Zheng, X.; Sun, Y.; Xie, J.; Sun, J.; Xue, W.; Zhou, G.; Wu, J.; Shi, F.; Zhang, R.; Zhu, Z.; So, K.; Cui, Y.; Li, J. *Energy Environ. Sci.* **2017**, *10*, 580−592.
(16) Wu, H.; Chan, G.; Choi, J. W.; Ryu, I.; Yao, Y.; McDowell, M. T.; Lee, S. W.; Jackson, A.; Yang, Y.; Hu, L.; Cui, Y. *Nat. Nanotechnol.* **2012**, *7*, 310−315.
(17) Wang, C.; Wu, H.; Chen, Z.; McDowell, M. T.; Cui, Y.; Bao, Z. *Nat. Chem.* **2013**, *5*, 1042−1048.
(18) Kovalenko, I.; Zdyrko, B.; Magasinski, A.; Hertzberg, B.; Milicev, Z.; Burtovyy, R.; Luzinov, I.; Yushin, G. *Science* **2011**, *334*, 75−79.
(19) Choi, S.; Kwon, T.-W.; Coskun, A.; Choi, J. *Science* **2017**, *357*, 279−283.
(20) Sheng, Y.; Fell, C. R.; Son, Y. K.; Metz, B. M.; Jiang, J.; Church, B. C. *Front. Energy Res.* **2014**, *2*, 56.
(21) Smekens, J.; Gopalakrishnan, R.; Steen, N. V.; Omar, N.; Hegazy, O.; Hubin, A.; Mierlo, J. V. *Energies* **2016**, *9*, 104.
(22) Novak, P.; Scheifele, W.; Winter, M.; Haas, O. *J. Power Sources* **1997**, *68*, 267−270.
(23) Schilcher, C.; Meyer, C.; Kwade, A. *Energy Technol.* **2016**, *4*, 1604−1610.
(24) Cho, Y.-S.; Yi, G.-R.; Kim, S.-H.; Pine, D.; Yang, S.-M. *Chem. Mater.* **2005**, *17*, 5006−5013.
(25) Son, I. H.; Park, J. H.; Kwon, S.; Park, S.; Rummeli, M. H.; Bachmatiuk, A.; Song, H. J.; Ku, J.; Choi, J. W.; Choi, J.; Doo, S.-G.; Chang, H. *Nat. Commun.* **2015**, *6*, 7393.
(26) Magasinski, A.; Dixon, P.; Hertzberg, B.; Kvit, A.; Ayala, J.; Yushin, G. *Nat. Mater.* **2010**, *9*, 353−358.
(27) Ruffo, R.; Hong, S. S.; Chan, C. K.; Huggins, R. A.; Cui, Y. *J. Phys. Chem. C* **2009**, *113*, 11390−11398.
(28) Lin, D.; Lu, Z.; Hsu, P.-C.; Lee, H. R.; Liu, N.; Zhao, J.; Wang, H.; Liu, C.; Cui, Y. *Energy Environ. Sci.* **2015**, *8*, 2371−2376.
(29) Jung, R.; Metzger, M.; Haering, D.; Solchenbach, S.; Marino, C.; Tsiouvaras, N.; Stinner, C.; Gasteiger, H. A. *J. Electrochem. Soc.* **2016**, *163*, A1705−A1716.
(30) Gauthier, M.; Mazouzi, D.; Reyter, D.; Lestriez, B.; Moreau, P.; Guyomard, D.; Roue, L. *Energy Environ. Sci.* **2013**, *6*, 2145−2155.
(31) Obrovac, M. N.; Chevrier, V. L. *Chem. Rev.* **2014**, *114*, 11444−11502.
(32) Jeong, S.; Lee, J.-P.; Ko, M.; Kim, G.; Park, S.; Cho, J. *Nano Lett.* **2013**, *13*, 3403−3407.
(33) Choi, J. W.; Hu, L.; Cui, L.; McDonough, J. R.; Cui, Y. *J. Power Sources* **2010**, *195*, 8311−8316.
(34) Chockla, A. M.; Harris, J. T.; Akhavan, V. A.; Bogart, T. D.; Holmberg, V. C.; Steinhagen, C.; Mullins, C. B.; Stevenson, K. J.; Korgel, B. A. *J. Am. Chem. Soc.* **2011**, *133*, 20914−20921.
(35) Wu, H.; Yu, G.; Pan, L.; Liu, N.; McDowell, M. T.; Bao, Z.; Cui, Y. *Nat. Commun.* **2013**, *4*, 1943.
(36) Xia, F.; Kim, S. B.; Cheng, H.; Lee, J. M.; Song, T.; Huang, Y.; Rogers, J. A.; Paik, U.; Park, W. I. *Nano Lett.* **2013**, *13*, 3340−3346.
(37) Song, J.; Chen, S.; Zhou, M.; Xu, T.; Lv, D.; Gordin, M. L.; Long, T.; Melnyk, M.; Wang, D. *J. Mater. Chem. A* **2014**, *2*, 1257−1262.
(38) Lee, J. I.; Choi, N. S.; Park, S. *Energy Environ. Sci.* **2012**, *5*, 7878−7882.

DOI: 10.1021/acs.nanolett.8b03065
Nano Lett. 2018, 18, 7060−7065